

Vibration Bandgap Analysis of Periodic Composite Microplates using Isogeometric Approach

Pengpeng LIU^{*,**}, Jianfang ZHOU^{*}, Shuohui YIN^{***}, Yan MEI^{**}

^{*}College of Mechanical and Electrical Engineering, Hohai University, Jiangsu 213000, PR China.

E-mail: zhoujf101@163.com

^{**}Chengdu Zoom Check Science & Technology Co., LTD, Sichuan 610052, PR China.

^{***}School of Mechanical Engineering and Mechanics, Xiangtan University, Hunan 411105, PR China.

E-mail: yinsh2016@163.com (Corresponding Author)

<https://doi.org/10.5755/j02.mech.33707>

1. Introduction

Periodic composite structures have been extensively studied [1-5] and used in energy harvesters, elastic wave filters and vibration isolators [6-8] due to the particular properties of band gap, which can prevent elastic waves from propagating in a specific frequency range. There are two kinds of formation mechanism of band gap [9]: local resonance and Bragg scattering. The vibration attenuation caused by the local vibration of the resonator can absorb the elastic wave energy [10]. The second case is elastic wave scattering that occurs at the interface of a material or structure [11]. However, in both cases the band gap characters are inherently microstructure-dependent [12], which is hard to be accurately captured by the classical elasto-dynamic theory. Therefore, it is necessary to use the higher-order elastic theory which includes microstructure-dependent material parameters to study the band gaps.

Recently, several size-dependent microbeam [13, 14] and microplate [15-18] elastic wave models have been developed based on higher-order continuum theory to investigate the band gaps. Liu et al. [19] studied the interface/surface stress effect on vibration band gap structure by surface elasticity theory. Li et al. [20] investigated the Bloch waves in the periodic laminated structure by using dipole gradient elasticity theory to describe microstructure effect. Zhang et al. [21, 22] developed a 2- and 3-dimensional periodic composites structure models for calculating band gaps of wave propagation using the modified coupled stress theory. After then, Zhang et al. [23] investigated the band gaps properties of periodic composite microplates by developing an Mindlin microplate contains both microstructure and surface energy effects. Zhang et al. [24-25] studied the wave propagation and tunable bandgaps of microbeam considered microstructure and magneto electro elastic effects.

All the above works are focus on solving the band gap of elastic wave problems by analytical solution. Xia et al. [26] and Lai et al. [27] established a 3-node triangular (T3) finite element method based on the modified couple stress theory (MCST) to investigate the microstructure effects on vibration band gap of periodic composite microplates. The higher order continuity is constructed by 9 nodal degrees of freedom [26, 27]. As the higher order continuity requirement in higher order elastic theory, more degrees of freedom [28, 29] or special technology [30, 31] are needed in traditional finite element method to establish the higher order gradient. To deal with the higher order gradient prob-

lem, a higher-order numerical approach based on the MCST is necessary to be developed for the vibration band gaps of periodic composite microplates. Isogeometric analysis (IGA) developed by Hughes et al. [32, 33] is a higher order computational approach, which uses high-order spline basis function for both geometric modeling and structure analysis. Therefore, the isogeometric analysis inherently satisfies the higher order continuity requirement of higher order elastic theory. In this paper, an isogeometric analysis method based on Mindlin and MCST is proposed for vibration band gaps in periodic composite microplates.

This paper will be divided into the following parts: The second part introduces the theoretical formula of band gap analysis based on MCST and Mindlin theory. The third part introduces the realization of isogeometric numerical method for periodic composite microplates. In the fourth part, numerical examples are given to investigate the vibration band gap problems. At the end of this paper, the main points are summarized.

2. Basic formulation

2.1. Periodic composite plate

Fig. 1 shows a periodic composite plate (domain) consisting of Phase I periodically embedded in Phase II. For the determination of the band gap in periodic composite plate, the plate structure is significantly larger than its unit cell, therefore a unit cell is considered and the periodic boundary condition is imposed on the cell. As shown in Fig. 1, the unit cell is a square with a square inclusion in the center. The geometry of the unit cell and inclusion are given in Fig. 1 with a and d .

Based on the Bloch theory for periodic media, the displacement field of the elastic wave problem can be described by harmonic function as:

$$\mathbf{u}(\mathbf{r}, t) = \mathbf{u}(\mathbf{r}) e^{i\omega t}, \quad (1)$$

where: $\mathbf{u}(\mathbf{r})$ is the spatial function; ω is the angular frequency. The position vector \mathbf{r} is used to represent the position of arbitrary point in the unit cell.

Based on the Bloch-Floquet theorem [34], the displacement field in Eq. (1) can be transformed as:

$$\mathbf{u}(\mathbf{r}, t) = \mathbf{u}_{\mathbf{k}}(\mathbf{r}) e^{i(\mathbf{k}\cdot\mathbf{r})}, \quad (2)$$

in which $\mathbf{u}_k(\mathbf{r})$ denotes a periodic function with the same material periodicity as region Π (namely $\mathbf{a}_i, i = 1, 2$); $\mathbf{k} = (k_x, k_y)$ represent the Bloch wave vector. Considered the material periodicity, the displacement field should satisfy the following periodic boundary conditions:

$$\begin{aligned} \mathbf{u}_k(\mathbf{r} + \mathbf{a}) &= \mathbf{u}_k \\ \mathbf{u}(\mathbf{r} + \mathbf{a}, \mathbf{k}) &= \mathbf{u}_k(\mathbf{r} + \mathbf{a}) e^{i(\mathbf{k} \cdot \mathbf{r})} e^{i(\mathbf{k} \cdot \mathbf{a})} \\ \mathbf{u}(\mathbf{r} + \mathbf{a}, \mathbf{k}) &= \mathbf{u}_k(\mathbf{r}) e^{i(\mathbf{k} \cdot \mathbf{a})} \end{aligned} \quad (3)$$

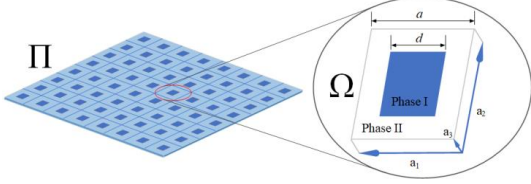


Fig. 1 Schematic of periodic bi-phase composite micro-plate and its unit cell

The relationships in Eq. (3) are the Bloch periodic boundary conditions which need imposed on the boundary of its unit cell.

2.2. Modified couple stress theory

For micro/nano periodic composite plate, the microstructure has great effect on the band gap character, therefore the MCST [35, 36] is employed to capture the microstructure effect of the unit cell in this work. Applying the MCST, the total strain energy of the unit cell can be expressed as:

$$U = \frac{1}{2} \int_{\Omega} (\boldsymbol{\sigma} : \boldsymbol{\varepsilon} + \mathbf{m} : \boldsymbol{\chi}) dV, \quad (4)$$

in which dV is a volume element; $\boldsymbol{\sigma}$ and \mathbf{m} are Cauchy stress tensor and couple stress tensor, respectively; $\boldsymbol{\varepsilon}$ is the infinitesimal strain tensor and $\boldsymbol{\chi}$ is the curvature tensor, provided as follows:

$$\boldsymbol{\varepsilon} = \frac{1}{2} (\nabla \mathbf{u} + (\nabla \mathbf{u})^T), \quad (5)$$

$$\boldsymbol{\chi} = \frac{1}{2} (\nabla \boldsymbol{\theta} + (\nabla \boldsymbol{\theta})^T), \quad (6)$$

$$\boldsymbol{\theta} = \frac{1}{2} \nabla \times \mathbf{u}, \quad (7)$$

where: $\boldsymbol{\theta}$ is the rotation vector.

According to the MCST, the constitutive relations can be written as:

$$\begin{aligned} \boldsymbol{\sigma} &= \lambda \text{tr}(\boldsymbol{\varepsilon}) \mathbf{I} + 2\mu \boldsymbol{\varepsilon} \\ \mathbf{m} &= 2\mu l^2 \boldsymbol{\chi} \end{aligned} \quad (8a-b)$$

in which, λ and μ are lamé constants; \mathbf{I} is unit tensor, and l is the material length parameter, which can be determined by experiment and used to represent the couple stress effect [36, 37].

The elastic wave propagation in solids is described by the elastic dynamic equations. Considered the microstructure effect, the unit cell governing equation based on the MCST and the Bloch boundary conditions are given as [23, 26]:

$$\begin{aligned} \nabla \cdot \boldsymbol{\sigma} - \frac{1}{2} \nabla \times (\nabla \cdot \mathbf{m}) - \frac{1}{2} \nabla \times \mathbf{c} + \mathbf{f} &= \rho \ddot{\mathbf{u}}, \\ \mathbf{u}(\mathbf{r} + \mathbf{a}, \mathbf{k}) &= \mathbf{u}_k(\mathbf{r}) e^{i(\mathbf{k} \cdot \mathbf{a})} \end{aligned} \quad (9a-b)$$

where: \mathbf{c} is the body couple moment and \mathbf{f} are the body force; ρ is the material density.

In order to facilitate the use of IGA to solve Bloch boundary value problem of unit cell, the weak form of Eqs. (9) without the external load can be transformed into its weak form as:

$$\int_T \int_{\Omega} \rho \ddot{\mathbf{u}} \cdot \delta \mathbf{u} dV dt + \int_T \int_{\Omega} (\boldsymbol{\sigma} : \delta \boldsymbol{\varepsilon} + \mathbf{m} : \delta \boldsymbol{\chi}) dV dt = 0 \quad (10a-b)$$

$$\mathbf{u}(\mathbf{r} + \mathbf{a}, \mathbf{k}) = \mathbf{u}_k(\mathbf{r}) e^{i(\mathbf{k} \cdot \mathbf{a})}$$

Eqs. (10a) represents the virtual work equation in the absence of any physical force and external load.

2.3. Mindlin plate theory

Based on the Mindlin plate theory [38], the displacement fields of the plate are defined as:

$$\begin{aligned} u(x, y, z) &= u_0(x, y) - z\varphi_x(x, y) \\ v(x, y, z) &= v_0(x, y) - z\varphi_y(x, y), \\ w(x, y, z) &= w_0(x, y) \end{aligned} \quad (11)$$

in which u_0, v_0, w_0 are the displacement of mid-plane in x, y and z directions, and φ_x, φ_y are the rotations.

Substituting the displacement field formula (11) into Eq. (5), the strain can be obtained as following:

$$\boldsymbol{\varepsilon} = \begin{Bmatrix} \varepsilon_x \\ \varepsilon_y \\ \gamma_{xy} \\ \gamma_{xz} \\ \gamma_{yz} \end{Bmatrix} = \begin{Bmatrix} \frac{\partial u_0}{\partial x} - z \frac{\partial \varphi_x}{\partial x} \\ \frac{\partial v_0}{\partial y} - z \frac{\partial \varphi_y}{\partial y} \\ \left(\frac{\partial u_0}{\partial y} + \frac{\partial v_0}{\partial x} \right) - z \left(\frac{\partial \varphi_x}{\partial y} + \frac{\partial \varphi_y}{\partial x} \right) \\ \frac{\partial w_0}{\partial x} - \varphi_x \\ \frac{\partial w_0}{\partial y} - \varphi_y \end{Bmatrix} = \begin{Bmatrix} \boldsymbol{\varepsilon}_m \\ \mathbf{0} \end{Bmatrix} + \begin{Bmatrix} -\boldsymbol{\varepsilon}_b \\ \boldsymbol{\varepsilon}_s \end{Bmatrix}, \quad (12)$$

where:

$$\boldsymbol{\varepsilon}_m = \begin{Bmatrix} \frac{\partial u_0}{\partial x} \\ \frac{\partial v_0}{\partial y} \\ \frac{\partial u_0}{\partial y} + \frac{\partial v_0}{\partial x} \end{Bmatrix}, \boldsymbol{\varepsilon}_b = \begin{Bmatrix} z \frac{\partial \varphi_x}{\partial x} \\ z \frac{\partial \varphi_y}{\partial y} \\ z \left(\frac{\partial \varphi_x}{\partial y} + \frac{\partial \varphi_y}{\partial x} \right) \end{Bmatrix}, \boldsymbol{\varepsilon}_s = \begin{Bmatrix} \frac{\partial w_0}{\partial x} - \varphi_x \\ \frac{\partial w_0}{\partial y} - \varphi_y \end{Bmatrix}. \quad (13)$$

Substituting Eqs. (12) and (13) into Eq. (8a) gives the stress tensor as:

$$\boldsymbol{\sigma} = \begin{Bmatrix} \sigma_x \\ \sigma_y \\ \sigma_{xy} \end{Bmatrix} = \mathbf{D}_m (\boldsymbol{\varepsilon}_m - \boldsymbol{\varepsilon}_b), \boldsymbol{\tau} = \begin{Bmatrix} \tau_{xz} \\ \tau_{yz} \end{Bmatrix} = \mathbf{D}_s \boldsymbol{\varepsilon}_s, \quad (14)$$

where:

$$\mathbf{D}_m = \frac{E}{1-\nu^2} \begin{bmatrix} 1 & \nu & 0 \\ \nu & 1 & 0 \\ 0 & 0 & (1-\nu)/2 \end{bmatrix}, \mathbf{D}_s = \frac{kE}{2(1+\nu)} \begin{bmatrix} 1 & 0 \\ 0 & 1 \end{bmatrix}, \quad (15)$$

in which E represent Young's modulus and ν is the Poisson's ratio; k is the shear coefficient which is set as $k = 5/6$.

Substituting the displacement field Eq. (11) into Eq. (7), the rotation vector is obtained as:

$$\boldsymbol{\theta} = \begin{Bmatrix} \theta_x \\ \theta_y \\ \theta_z \end{Bmatrix} = \frac{1}{2} \begin{bmatrix} \frac{\partial w_0}{\partial y} + \varphi_y \\ -\frac{\partial w_0}{\partial x} - \varphi_x \\ \frac{\partial v_0}{\partial x} - \frac{\partial u_0}{\partial y} + z \frac{\partial \varphi_x}{\partial y} - z \frac{\partial \varphi_y}{\partial x} \end{bmatrix}. \quad (16)$$

According to Eqs. (6) and (16), the symmetric curvature tensor is:

$$\boldsymbol{\chi} = \begin{Bmatrix} \chi_x \\ \chi_y \\ \chi_z \\ \chi_{xy} \\ \chi_{xz} \\ \chi_{yz} \end{Bmatrix} = \begin{bmatrix} \frac{1}{2} \left(\frac{\partial^2 w_0}{\partial y \partial x} + \frac{\partial \varphi_y}{\partial x} \right) \\ -\frac{1}{2} \left(\frac{\partial^2 w_0}{\partial x \partial y} + \frac{\partial \varphi_x}{\partial y} \right) \\ -\frac{1}{2} \left(\frac{\partial \varphi_y}{\partial x} - \frac{\partial \varphi_x}{\partial y} \right) \\ \frac{1}{4} \left(\frac{\partial^2 w_0}{\partial y^2} + \frac{\partial \varphi_y}{\partial y} \right) - \frac{1}{4} \left(\frac{\partial^2 w_0}{\partial x^2} + \frac{\partial \varphi_x}{\partial x} \right) \\ \frac{1}{4} \left(\frac{\partial^2 v_0}{\partial x^2} - \frac{\partial^2 u_0}{\partial x \partial y} \right) - z \frac{1}{4} \left(\frac{\partial^2 \varphi_y}{\partial x^2} - \frac{\partial^2 \varphi_x}{\partial y \partial x} \right) \\ \frac{1}{4} \left(\frac{\partial^2 v_0}{\partial x \partial y} - \frac{\partial^2 u_0}{\partial y^2} \right) - z \frac{1}{4} \left(\frac{\partial^2 \varphi_y}{\partial x \partial y} - \frac{\partial^2 \varphi_x}{\partial y^2} \right) \end{bmatrix} = \begin{bmatrix} \chi_\alpha \\ \chi_\beta \end{bmatrix} + \begin{bmatrix} \mathbf{0} \\ -z \boldsymbol{\chi}_\gamma \end{bmatrix}, \quad (17)$$

where:

$$\boldsymbol{\chi}_\alpha = \begin{bmatrix} \frac{1}{2} \left(\frac{\partial^2 w_0}{\partial y \partial x} + \frac{\partial \varphi_y}{\partial x} \right) \\ -\frac{1}{2} \left(\frac{\partial^2 w_0}{\partial x \partial y} + \frac{\partial \varphi_x}{\partial y} \right) \\ -\frac{1}{2} \left(\frac{\partial \varphi_y}{\partial x} - \frac{\partial \varphi_x}{\partial y} \right) \\ \frac{1}{4} \left(\frac{\partial^2 w_0}{\partial y^2} + \frac{\partial \varphi_y}{\partial y} \right) - \frac{1}{4} \left(\frac{\partial^2 w_0}{\partial x^2} + \frac{\partial \varphi_x}{\partial x} \right) \end{bmatrix}, \quad (18a)$$

$$\boldsymbol{\chi}_\beta = \begin{bmatrix} \frac{1}{4} \left(\frac{\partial^2 v_0}{\partial x^2} - \frac{\partial^2 u_0}{\partial x \partial y} \right) \\ \frac{1}{4} \left(\frac{\partial^2 v_0}{\partial x \partial y} - \frac{\partial^2 u_0}{\partial y^2} \right) \end{bmatrix}, \quad (18b)$$

$$\boldsymbol{\chi}_\gamma = \begin{bmatrix} \frac{1}{4} \left(\frac{\partial^2 \varphi_y}{\partial x^2} - \frac{\partial^2 \varphi_x}{\partial y \partial x} \right) \\ \frac{1}{4} \left(\frac{\partial^2 \varphi_y}{\partial x \partial y} - \frac{\partial^2 \varphi_x}{\partial y^2} \right) \end{bmatrix}. \quad (18c)$$

From Eqs. (17), (18) and (8b), the expression of couple stress can be obtained as:

$$\mathbf{m} = \begin{bmatrix} \mathbf{m}_1 \\ \mathbf{m}_2 \end{bmatrix} = \begin{bmatrix} \mathbf{D}_c & \mathbf{0} \\ \mathbf{0} & \mathbf{D}_p \end{bmatrix} \begin{bmatrix} \boldsymbol{\chi}_\alpha \\ \boldsymbol{\chi}_\beta - z \boldsymbol{\chi}_\gamma \end{bmatrix} = \frac{El^2}{(1+\nu)} \begin{bmatrix} \chi_x \\ \chi_y \\ \chi_z \\ \chi_{xy} \\ \chi_{xz} \\ \chi_{yz} \end{bmatrix}, \quad (19)$$

where:

$$\mathbf{m}_1 = \mathbf{D}_c \boldsymbol{\chi}_\alpha, \mathbf{m}_2 = \mathbf{D}_p (\boldsymbol{\chi}_\beta - z \boldsymbol{\chi}_\gamma), \quad (20a)$$

with

$$\mathbf{D}_c = \frac{El^2}{(1+\nu)} \begin{bmatrix} 1 & 0 & 0 & 0 \\ 0 & 1 & 0 & 0 \\ 0 & 0 & 1 & 0 \\ 0 & 0 & 0 & 1 \end{bmatrix}, \mathbf{D}_p = \frac{El^2}{(1+\nu)} \begin{bmatrix} 1 & 0 \\ 0 & 1 \end{bmatrix}, \quad (20b-c)$$

3. Isogeometric analysis approach

3.1. Introduction to NURBS basis functions

The Non-Uniform Rational B-Splines (NURBS) basis functions can be established from B-splines basis functions. The one-dimensional NURBS basis function is provided as follows [33]:

$$R_{i,p}(\xi) = \frac{N_{i,p}(\xi) w_i}{\sum_{j=1}^{\bar{n}} N_{j,p}(\xi) w_j}, \quad (21)$$

where: $N_{i,p}(\xi)$ is the B-spline basis function; w_i represents the i^{th} weight; ξ denotes the parametric coordinate; p is the degree of the basis function; \bar{n} represents the number of control points and corresponding basic functions.

The one-dimensional B-spline basis function for a given knot vector $\xi = \{\xi_1, \xi_2, \dots, \xi_{n+p+1}\}$ ($\xi_i < \xi_{i+1}$) is defined as [33]:

$$N_{i,0}(\xi) = \begin{cases} 1 & \text{if } \xi_i \leq \xi < \xi_{i+1} \\ 0 & \text{otherwise} \end{cases} \text{ for } p=0, \quad (22a)$$

$$N_{i,p}(\xi) = \frac{\xi - \xi_i}{\xi_{i+p} - \xi_i} N_{i,p-1}(\xi) + \frac{\xi_{i+p+1} - \xi}{\xi_{i+p+1} - \xi_{i+1}} N_{i+1,p-1}(\xi) \text{ for } p \geq 1. \quad (22b)$$

Two directions B-spline basis functions can construct the two-dimensional NURBS basis functions as:

$$R_{i,j}^{p,q}(\xi, \eta) = \frac{N_{i,p}(\xi) N_{j,q}(\eta) w_{i,j}}{\sum_{i=1}^{\bar{n}} \sum_{j=1}^{\bar{m}} N_{i,p}(\xi) N_{j,q}(\eta) w_{i,j}}, \quad (23)$$

where: $N_{i,p}(\xi)$ and $N_{j,q}(\eta)$ are the B-spline basic functions with degree of p , and q in the ξ and η directions, respectively; $w_{i,j}$ is the 2D weight.

3.2. Isogeometric analysis discretization equations

Based on the Mindlin plate theory and isogeometric analysis, the displacement can be approximated by the NURBS basis function as:

$$\mathbf{u}^h = \sum_{I=1}^{NP} R_I \mathbf{u}_I, \quad (24)$$

in which $NP=(p+1)(q+1)$ represents the number of control points in the element; \mathbf{u}_I and R_I represent the displacement of control point I and shape function, respectively.

Based on the Mindlin plate theory and isogeometric analysis, the displacement can be approximated by the NURBS basis function as:

$$\mathbf{u}_I = [\mathbf{u}_I \ \mathbf{v}_I \ \mathbf{w}_I \ \varphi_{xI} \ \varphi_{yI}]^T. \quad (25)$$

It can be seen from Fig. 1 that the unit cell contains square inclusion. In order to describe the material interface, the level set method (LSM) [39] is employed to capture the interface curve and then a triangular sub-domain technique [40] is used to improve the accuracy of elements cut by interface curve.

Substituting Eq. (24) into Eq. (13) gives the following:

$$\boldsymbol{\varepsilon}_m = \sum_{I=1}^{NP} \mathbf{B}_I^m \mathbf{u}_I, \boldsymbol{\varepsilon}_b = z \sum_{I=1}^{NP} \mathbf{B}_I^b \mathbf{u}_I, \boldsymbol{\varepsilon}_s = \sum_{I=1}^{NP} \mathbf{B}_I^s \mathbf{u}_I, \quad (26)$$

where:

$$\mathbf{B}_I^m = \begin{bmatrix} R_{I,x} & 0 & 0 & 0 & 0 \\ 0 & R_{I,y} & 0 & 0 & 0 \\ R_{I,y} & R_{I,x} & 0 & 0 & 0 \end{bmatrix}, \quad (27a)$$

$$\mathbf{B}_I^b = \begin{bmatrix} 0 & 0 & 0 & R_{I,x} & 0 \\ 0 & 0 & 0 & 0 & R_{I,y} \\ 0 & 0 & 0 & R_{I,y} & R_{I,x} \end{bmatrix}, \quad (27b)$$

$$\mathbf{B}_I^s = \begin{bmatrix} 0 & 0 & R_{I,x} & -R_I & 0 \\ 0 & 0 & R_{I,y} & 0 & -R_I \end{bmatrix}. \quad (27c)$$

Substituting Eq. (24) into Eq. (18a-c) gives the following:

$$\boldsymbol{\chi}_\alpha = \sum_{I=1}^{NP} \mathbf{B}_I^\alpha \mathbf{u}_I, \boldsymbol{\chi}_\beta = \sum_{I=1}^{NP} \mathbf{B}_I^\beta \mathbf{u}_I, \boldsymbol{\chi}_\gamma = \sum_{I=1}^{NP} \mathbf{B}_I^\gamma \mathbf{u}_I, \quad (28)$$

where:

$$\mathbf{B}_I^\alpha = \begin{bmatrix} 0 & 0 & \frac{1}{2} R_{I,yx} & 0 & \frac{1}{2} R_{I,x} \\ 0 & 0 & -\frac{1}{2} R_{I,xy} & -\frac{1}{2} R_{I,y} & 0 \\ 0 & 0 & 0 & \frac{1}{2} R_{I,y} & -\frac{1}{2} R_{I,x} \\ 0 & 0 & \frac{1}{4} (R_{I,yy} - R_{I,xx}) & -\frac{1}{4} R_{I,x} & \frac{1}{4} R_{I,y} \end{bmatrix}, \quad (29a)$$

$$\mathbf{B}_I^\beta = \begin{bmatrix} -\frac{1}{4} R_{I,xy} & \frac{1}{4} R_{I,xx} & 0 & 0 & 0 \\ -\frac{1}{4} R_{I,yy} & \frac{1}{4} R_{I,xy} & 0 & 0 & 0 \end{bmatrix}, \quad (29b)$$

$$\mathbf{B}_I^\gamma = \begin{bmatrix} 0 & 0 & 0 & -\frac{1}{4} R_{I,yx} & \frac{1}{4} R_{I,xx} \\ 0 & 0 & 0 & -\frac{1}{4} R_{I,yy} & \frac{1}{4} R_{I,xy} \end{bmatrix}. \quad (29c)$$

The vibration band gap of unit cell is calculated by

modal analysis. The matrix form of the unit cell virtual work Eq. (10a) can be written as:

$$\int_T \int_{\Omega} \delta \begin{bmatrix} \boldsymbol{\varepsilon}_m - \boldsymbol{\varepsilon}_b \\ \boldsymbol{\varepsilon}_s \end{bmatrix}^T \begin{bmatrix} \mathbf{D}_m & \mathbf{0} \\ \mathbf{0} & \mathbf{D}_s \end{bmatrix} \begin{bmatrix} \boldsymbol{\varepsilon}_m - \boldsymbol{\varepsilon}_b \\ \boldsymbol{\varepsilon}_s \end{bmatrix} + \delta \begin{bmatrix} \boldsymbol{\chi}_\alpha \\ \boldsymbol{\chi}_\beta - z\boldsymbol{\chi}_\gamma \end{bmatrix}^T \begin{bmatrix} \mathbf{D}_c & \mathbf{0} \\ \mathbf{0} & \mathbf{D}_p \end{bmatrix} \begin{bmatrix} \boldsymbol{\chi}_\alpha \\ \boldsymbol{\chi}_\beta - z\boldsymbol{\chi}_\gamma \end{bmatrix} dV dt = \int_T \int_{\Omega} \rho \delta \mathbf{u}^T \cdot \ddot{\mathbf{u}} dV dt. \quad (30)$$

The harmonic equation of displacement field \mathbf{u} introduced into Eq. (30) to obtain the governing equation as follows:

$$[\mathbf{K} - \omega^2 \mathbf{M}] \mathbf{u}_0 = 0, \quad (31)$$

$$\mathbf{K} = \int_{\Omega} \delta \begin{bmatrix} \mathbf{B}_I^m - z\mathbf{B}_I^b \\ \mathbf{B}_I^s \end{bmatrix}^T \begin{bmatrix} \mathbf{D}_m & \mathbf{0} \\ \mathbf{0} & \mathbf{D}_s \end{bmatrix} \begin{bmatrix} \mathbf{B}_I^m - z\mathbf{B}_I^b \\ \mathbf{B}_I^s \end{bmatrix} + \delta \begin{bmatrix} \mathbf{B}_I^\alpha \\ \mathbf{B}_I^\beta - z\mathbf{B}_I^\gamma \end{bmatrix}^T \begin{bmatrix} \mathbf{D}_c & \mathbf{0} \\ \mathbf{0} & \mathbf{D}_p \end{bmatrix} \begin{bmatrix} \mathbf{B}_I^\alpha \\ \mathbf{B}_I^\beta - z\mathbf{B}_I^\gamma \end{bmatrix} dV. \quad (32)$$

\mathbf{M} is the mass matrix which can be written as:

$$\mathbf{M} = \int_{\Omega} \mathbf{N}^T \begin{bmatrix} \rho & 0 & 0 & 0 & 0 \\ 0 & \rho & 0 & 0 & 0 \\ 0 & 0 & \rho & 0 & 0 \\ 0 & 0 & 0 & z^2 \rho & 0 \\ 0 & 0 & 0 & 0 & z^2 \rho \end{bmatrix} \mathbf{N} dV, \quad (33)$$

where:

$$\mathbf{N} = \begin{bmatrix} R_I & 0 & 0 & 0 & 0 \\ 0 & R_I & 0 & 0 & 0 \\ 0 & 0 & R_I & 0 & 0 \\ 0 & 0 & 0 & R_I & 0 \\ 0 & 0 & 0 & 0 & R_I \end{bmatrix}. \quad (34)$$

3.3. Implementation of Bloch periodic boundary conditions

Now, the Bloch periodic boundary conditions are considered and implemented on the unit cell. Fig. 2 shows the periodic bi-phase composite microplate unit cell and the classification of nodes. a_1 and a_2 are the lengths of the unit cell. The boundary node displacement on the cell are classified by 4 edge nodes and 4 corner nodes. The positions of 4 corner nodes, \mathbf{u}_{TL} , \mathbf{u}_{TR} , \mathbf{u}_{BL} , and \mathbf{u}_{BR} , are shown in Fig. 2. And, \mathbf{u}_L , \mathbf{u}_R , \mathbf{u}_T and \mathbf{u}_B denote the left, right, top and bottom edge displacements of the unit cell, respectively. Node displacements located inside of the unit cell are represented by \mathbf{u}_{IN} .

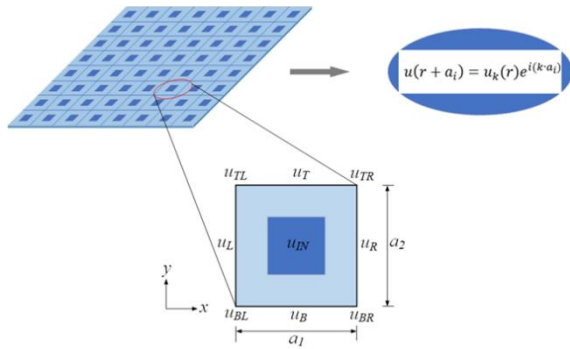


Fig. 2 Schematic of bi-phase unit cell microstructure and the classification of nodes

Therefore, by considering the Bloch periodic boundary condition Eq. (3), the relationship between the independent node displacement vector and the entire node displacement vector can be written as [23]:

where: \mathbf{u}_0 is the displacement of the unit cell; \mathbf{K} is the total stiffness matrix, expressed as:

$$\mathbf{u} = \begin{bmatrix} \mathbf{u}_{IN} \\ \mathbf{u}_L \\ \mathbf{u}_R \\ \mathbf{u}_B \\ \mathbf{u}_T \\ \mathbf{u}_{BL} \\ \mathbf{u}_{BR} \\ \mathbf{u}_{TR} \\ \mathbf{u}_{TL} \end{bmatrix} = \begin{bmatrix} \mathbf{I} & 0 & 0 & 0 \\ 0 & \mathbf{I} & 0 & 0 \\ 0 & \lambda_1 \mathbf{I} & 0 & 0 \\ 0 & 0 & \mathbf{I} & 0 \\ 0 & 0 & \lambda_2 \mathbf{I} & 0 \\ 0 & 0 & 0 & \mathbf{I} \\ 0 & 0 & 0 & \lambda_1 \mathbf{I} \\ 0 & 0 & 0 & \lambda_1 \lambda_2 \mathbf{I} \\ 0 & 0 & 0 & \lambda_2 \mathbf{I} \end{bmatrix} \begin{bmatrix} \mathbf{u}_{IN} \\ \mathbf{u}_L \\ \mathbf{u}_B \\ \mathbf{u}_{BL} \end{bmatrix} = \mathbf{P} \tilde{\mathbf{u}}, \quad (35)$$

where: $\lambda_1 = e^{ik \cdot a_1}$, $\lambda_2 = e^{ik \cdot a_2}$, $\tilde{\mathbf{u}}$ represent the independent node displacements of \mathbf{u}_{IN} , \mathbf{u}_L , \mathbf{u}_B , and \mathbf{u}_{BL} . \mathbf{I} is the identity matrix; \mathbf{P} denotes the transformation matrix which represent the periodic relationship and reduce the degrees of freedom effectively.

Substitute Eq. (35) into Eq. (31) to obtain as:

$$[\mathbf{K} - \omega^2 \mathbf{M}] \mathbf{P} \tilde{\mathbf{u}} = 0. \quad (36)$$

Given the conjugate transpose \mathbf{P}^* of \mathbf{P} , Eq. (36) can be written as:

$$\mathbf{P}^* [\mathbf{K} - \omega^2 \mathbf{M}] \mathbf{P} \tilde{\mathbf{u}} = 0. \quad (37)$$

Therefore, we have the final form of the governing equation by considering the Bloch boundary conditions as follows:

$$[\mathbf{K}_r - \omega^2 \mathbf{M}_r] \tilde{\mathbf{u}} = 0, \quad (38)$$

where:

$$\mathbf{K}_r = \mathbf{P}^* \mathbf{K} \mathbf{P}, \quad \mathbf{M}_r = \mathbf{P}^* \mathbf{M} \mathbf{P}. \quad (39)$$

4. Numerical examples

At this work, the band gap analysis of periodic composite microplate considering microstructure effect will be investigated by the isogeometric analysis based on MCST. Firstly, the accuracy and effective of the present method is validated in the first example by comparison with analytical results [23]. Then, the influence of microstructure effect, volume fraction and the length of unit cell on the band gap in microplate are studied in details.

4.1. Comparison and validation

To validate the present approach, a bi-phase unit cell problem is considered here. The geometry of the unit cell with a square inclusion are $a = 1$ mm, $d = 0.4$ mm, and thickness $h = 120$ μm . The unit cell is discretized by NURBS isogeometric analysis with cubic degree NURBS basis function. As described in Fig. 1, the inclusion material I and the matrix material II is assume to be iron and epoxy, respectively. Both material properties are provided in Table 1 and used in the rest of this work. Besides, the material length parameter l is obtained by $l = \frac{b_h}{\sqrt{3(1-\nu)}}$ [41, 42] with

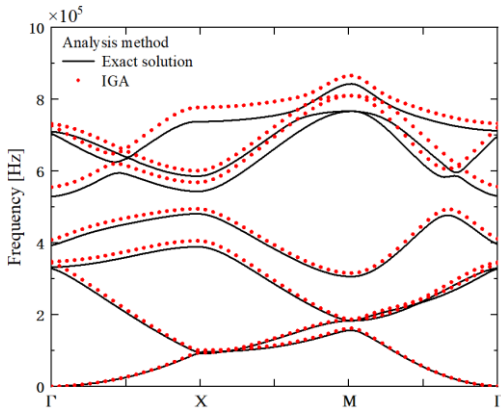
higher-order bending parameter b_h and Poisson's ratio ν . The band diagram results obtained by IGA and exact solution are given in Fig. 3. The band diagrams Figs. 3, a, b are

obtained by IGA with 19×19 and 29×29 control points mesh, respectively, given in Fig. 4. Fig. 3 shows that the IGA results are match with exact solution results, especially in the lower frequency. In higher frequencies, the IGA results are slightly above the exact results, but with tolerable differences. Compared Fig. 3, a and b, the IGA results obtained by 29×29 mesh is closed to exact results than the results obtained by 19×19 mesh. As the difference between the results of the IGA with refined mesh and the exact solution is very small, in the rest of the paper, the 29×29 mesh is employed.

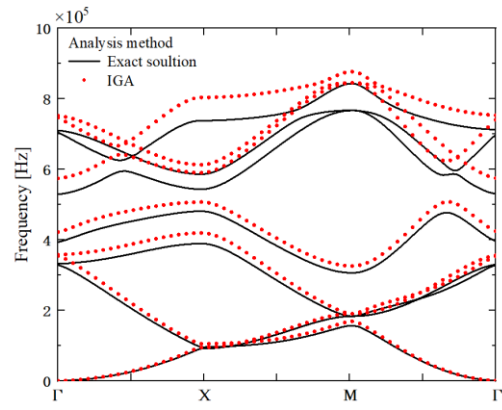
Table 1

The material properties of the unit cell

Material	E , GPa	ν	l , μm	ρ , g/cm^3
Iron	177.33	0.27	6.76	7
Epoxy	3.3	0.33	16.93	1.18

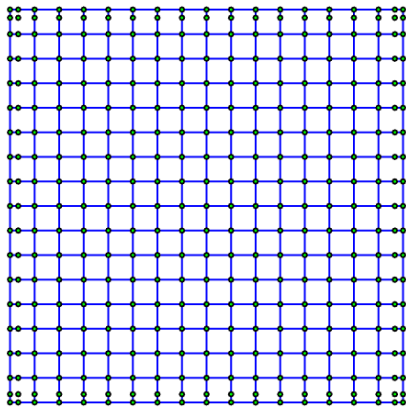


a) Band gap by IGA with 19×19 mesh

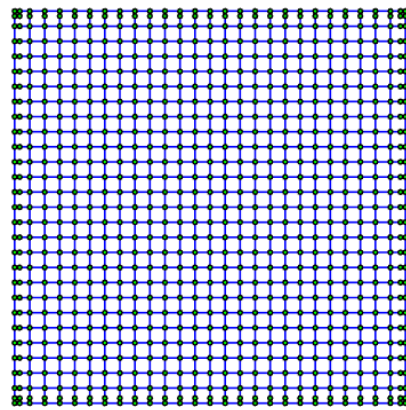


b) Band gap by IGA with 29×29 mesh

Fig. 3 A comparison of band gap between exact solution and IGA



a) 19×19 mesh



b) 29×29 mesh

Fig. 4 A comparison of band gap between exact solution and IGA

4.2. Effect of the microstructure

This example is aimed to investigate the influence of the microstructure on the vibration band gap of unit cell. The same geometry and material properties as above are used here with square unit cell $a = 1$ mm and square inclusion of $d = 0.4$ mm. Fig. 5 shows the first vibration band gaps obtained by the IGA based on classical plate theory (classical) and non-classical plate theory (that is MCST) for different unit cell thickness $h = 20$ μm , $h = 60$ μm and $h = 120$ μm . The first band gaps obtained by IGA based on classical plate theory are: 95.658-111.880 kHz for $h = 20$ μm , 270.497-313.089 kHz for $h = 60$ μm , 475.892-

535.945 kHz for $h = 120$ μm . However, the band gaps obtained by IGA based on non-classical plate theory are: 177.846-197.817 kHz for $h = 20$ μm , 307.694-351.652 kHz for $h = 60$ μm , 495.099-555.732 kHz for $h = 120$ μm .

It can be seen from Fig. 5 that the obtained band gap values increased as the thickness h increasing for both the classical theory and MCST. On the other hand, the difference between the IGA based on classical theory and MCST theory is decreased as the thickness increasing. This observation prove that the microstructure effect has significant influence on the vibration band gaps for very thin plates only.

4.3. Effect of the unit cell length

This example investigated the effect of the square unit cell length a . The thickness $h = 20 \mu\text{m}$ and $d = 0.4a$ are used in the present example. The first band gaps calculated by IGA based on MCST for the periodic composite microplate of different length $a = 20h, 40h, 100h$ and $200h$ are given in

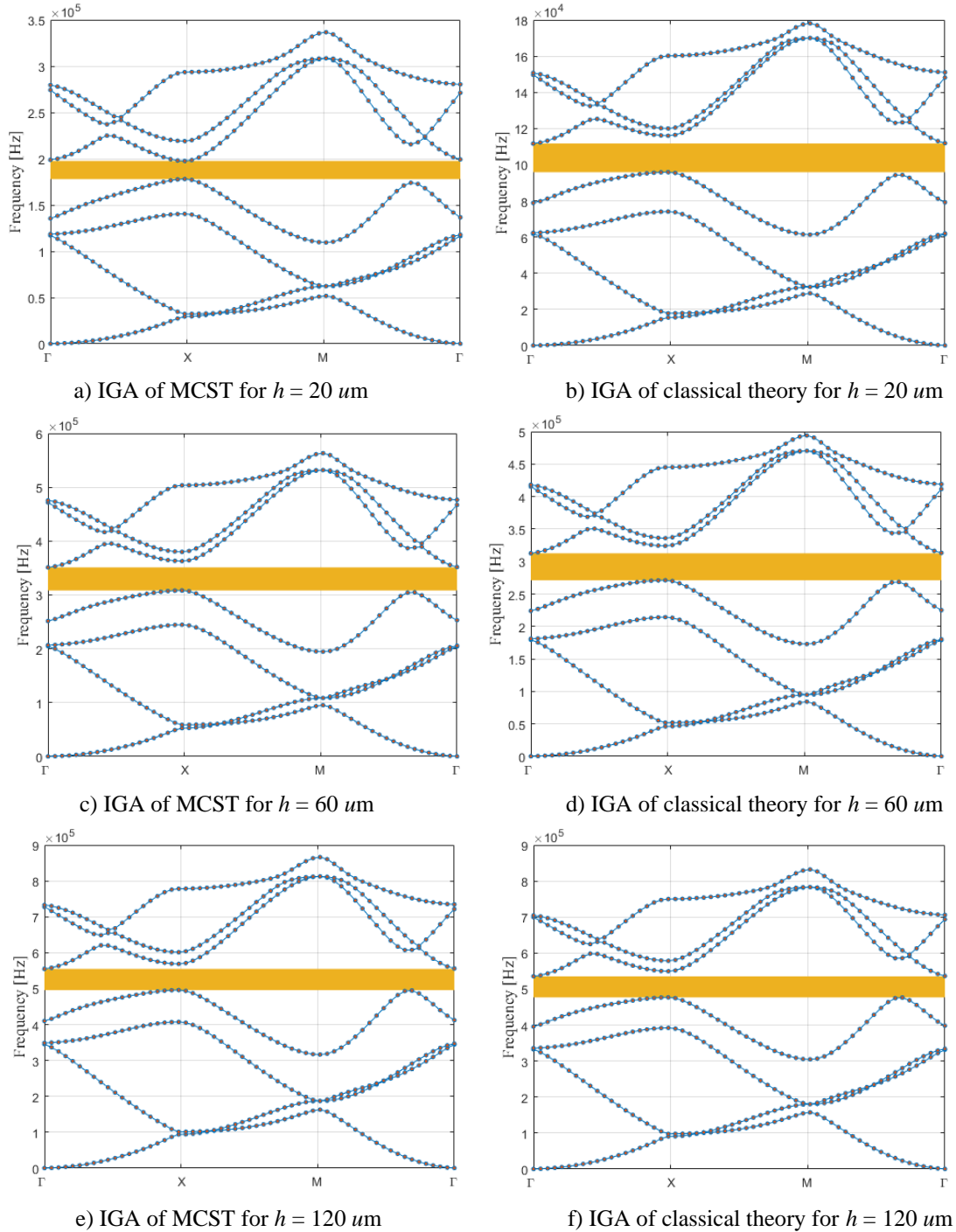


Fig. 5 The influence of microstructure on the vibration band gaps

4.4. Effect of volume fraction of the inclusion

To investigate the influence of volume fraction of the inclusion on the band gaps, a new example is presented. A vibration band gap analysis for unit cell with the length of inclusion $d = 0.4a, 0.5a$ and $0.6a$ are considered here. The unit cell square matrix with length $a = 1 \text{ mm}$ and thickness $h = 20 \mu\text{m}$ are used. Fig. 7 display the first band gaps for

Fig. 6. The first band gaps value for $a = 20h, 40h, 100h$ and $200h$ are 1041.389-1139.204 kHz (band gap 97.815 kHz), 275.084-305.930 kHz (band gap 30.845 kHz), 45.277-50.393 kHz (band gap 5.116 kHz) and 11.412-12.734 kHz (band gap 1.322 kHz), respectively. It can be observed that the frequencies and band gap width decreased as the square unit cell length a increasing.

different length of d obtained by IGA based on MCST. The first band gap is 177.846-197.817 kHz (band gap 19.971 kHz), 207.779-229.487 kHz (band gap 23.158 kHz) and 238.399-240.615 kHz (band gap 2.216 kHz) for $d = 0.4a, 0.5a$ and $0.6a$ respectively. The results indicated that the width of band gap increases firstly and then decreases as the size of inclusion increasing.

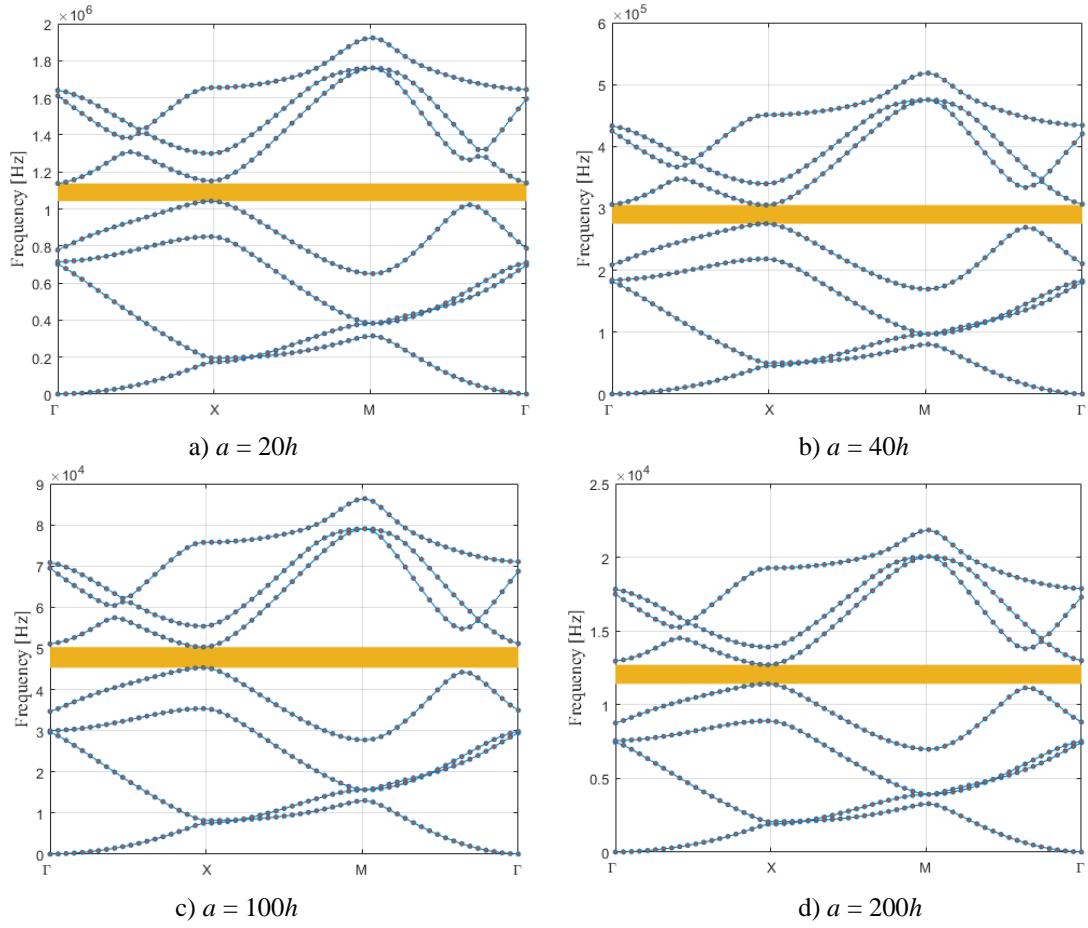


Fig. 6 The vibration band gaps for different unit cell length a

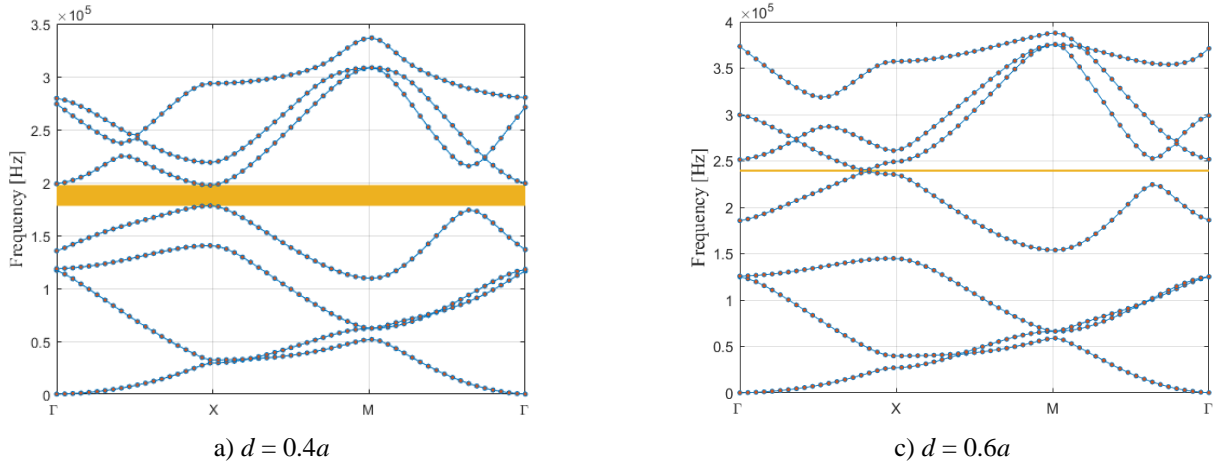
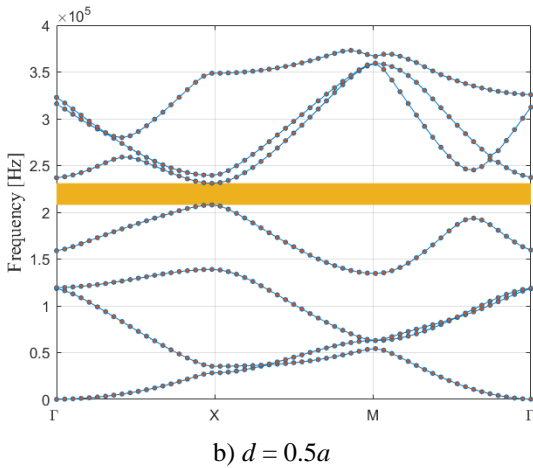


Fig. 7 The first band gaps for different d



5. Conclusions

In this work, an isogeometric analysis approach combined with Mindlin theory and MCST is proposed for the vibration band gap analysis of periodic composite microplates. The microstructure effect is considered by MCST, and the higher order continuity is easily satisfied in the framework of NURBS based isogeometric analysis. The elasto-dynamics and discrete equations of isogeometric analysis are obtained under the Mindlin kinematics assumptions. The present approach is validated by comparison with analytical solution, and the influence of microstructure effect, volume fraction and unit cell length on the first band gap is investigated in details. Some conclusions are as follows:

1. An isogeometric analysis approach based on Mindlin theory and MCST is developed for band gap analysis of periodic composite structures.
2. The microstructure effect has significant influence on the vibration band gap for very thin plates only.
3. The band gap frequencies and width decrease as the unit cell length a increasing.
4. The width of band gap first increases and then decreases as the size of inclusion increasing.

5. References

1. **Hsu, J. C.; Wu, T. T.** 2006. Efficient formulation for band-structure calculations of two-dimensional phononic-crystal plates, *Phys. Rev. B.* 74: 144303. <https://doi.org/10.1103/PhysRevB.74.144303>.
2. **Kushwaha, M. S.; Halevi, P.; Dobrzynski, L.; Djafari-Rouhani, B.** 1993. Acoustic band structure of periodic elastic composites, *Phys. Rev. Lett.* 71: 2022-2025. <https://doi.org/10.1103/PhysRevLett.71.2022>.
3. **Liu, X.; Shi, Z.; Mo, Y. L.** 2016. Attenuation zones of initially stressed periodic Mindlin plates on an elastic foundation, *Int. J. Mech. Sci.* 115-116: 12-23. <https://doi.org/10.1016/j.ijmecsci.2016.06.010>.
4. **Sigalas, M. M.; Economou, E. N.** 1994. Elastic waves in plates with periodically placed inclusions, *J. Appl. Phys.* 75: 2845-2850. <https://doi.org/10.1063/1.356177>.
5. **Chin, E. B.; Mokhtari, A. A.; Srivastava, A.; Sukumar, N.** 2021. Spectral extended finite element method for band structure calculations in phononic crystals, *J. Comput. Phys.* 427: 110066. <https://doi.org/10.1016/j.jcp.2020.110066>.
6. **Matlack, K. H.; Bauhofer, A.; Krödel, S.; Palermo, A.; Daraio, C.** 2016. Composite 3D-printed metastructures for low-frequency and broadband vibration absorption, *Proc. Natl. Acad. Sci. U.S.A.* 113: 8386-8390. <https://doi.org/10.1073/pnas.1600171113>.
7. **Wang, P.; Shim, J.; Bertoldi, K.** 2013. Effects of geometric and material nonlinearities on tunable band gaps and low-frequency directionality of phononic crystals, *Phys. Rev. B.* 88: 014304. <https://doi.org/10.1103/physrevb.88.014304>.
8. **Khelif, A.; Choujaa, A.; Benchabane, S.; Djafari-Rouhani, B.; Laude, V.** 2004. Guiding and bending of acoustic waves in highly confined phononic crystal waveguides, *Appl. Phys. Lett.* 84: 4400-4402. <https://doi.org/10.1063/1.1757642>.
9. **Chen, Y.; Wang, L.** 2014. Periodic co-continuous acoustic metamaterials with overlapping locally resonant and Bragg band gaps, *Appl. Phys. Lett.* 105: 191907. <https://doi.org/10.1063/1.4902129>.
10. **Krushynska, A. O.; Miniaci, M.; Kouznetsova, V. G.; Geers, Marc, G. D.** 2017. Multilayered inclusions in locally resonant metamaterials: Two-dimensional versus three-dimensional modeling, *J. Vib. Acoust.* 139: 024501. <https://doi.org/10.1115/1.4035307>.
11. **Krushynska, A. O.; Miniaci, M.; Bosia, F.; Pugno, N.M.** 2017. Coupling local resonance with Bragg band gaps in single-phase mechanical metamaterials, *Extreme. Mech. Lett.* 12: 30-36. <https://doi.org/10.1016/j.eml.2016.10.004>.
12. **Kadic, M.; Frenzel, T. Wegener, M.** 2018. When size matters, *Nat. Phys.* 14: 8-9. <https://doi.org/10.1038/nphys4287>.
13. **Rostami, R.; Mohammadimehr, M.; Ghannad, M.; Jalali, A.** 2018. Forced vibration analysis of nano-composite rotating pressurized microbeam reinforced by CNTs based on MCST with temperature-variable material properties, *Theor. Appl. Mech. Lett.* 8: 97-108. <https://doi.org/10.1016/j.taml.2018.02.005>.
14. **Jena, S. K.; Mundari, R.; Chakraverty, S.** 2021. Vibration of microstructural elements. *New Paradigms in Computational Modeling and Its Applications*, p. 35-44. <https://doi.org/10.1016/B978-0-12-822133-4.00013-X>.
15. **Hou, D.; Wang, L.; Yan, J.; Liew, K. M.** 2022. Vibration analysis of a strain gradient plate model via a mesh-free moving Kriging Interpolation Method, *Eng. Anal. Bound. Elem.* 135: 156-166. <https://doi.org/10.1016/j.enganabound.2021.11.014>.
16. **Markolefas, S.; Fafalis, D.** 2021. Strain gradient theory based dynamic mindlin-reissner and kirchhoff microplates with microstructural and micro-inertial effects. *Geodynamics 1*: 49-94. <https://doi.org/10.3390/dynamics1010005>.
17. **Mousavi, S. M.; Paavola, J.** 2014. Analysis of plate in second strain gradient elasticity, *Arch. Appl. Mech.* 84: 1135-1143. <https://doi.org/10.1007/s00419-014-0871-9>.
18. **Chen, W.; Li, X.** 2014. A new modified couple stress theory for anisotropic elasticity and microscale laminated Kirchhoff plate model, *Arch. Appl. Mech.* 84: 323-341. <https://doi.org/10.1007/s00419-013-0802-1>.
19. **Liu, W.; Chen, J.; Liu, Y.; Su, X.** 2012. Effect of interface/surface stress on the elastic wave band structure of two-dimensional phononic crystals, *Phys. Lett. A.* 376: 605-609. <https://doi.org/10.1016/j.physleta.2011.11.043>.
20. **Li, Y.; Wei, P.; Zhou, Y.** 2016. Band gaps of elastic waves in 1-D phononic crystal with dipolar gradient elasticity, *Acta. Mech.* 227: 1005-1023. <https://doi.org/10.1007/s00707-015-1495-z>.
21. **Zhang, G. Y.; Gao, X. L.** 2018. Elastic wave propagation in 3-D periodic composites: band gaps incorporating microstructure effect, *Compos. Struct.* 204: 920-932. <https://doi.org/10.1016/j.compstruct.2018.07.115>.
22. **Zhang, G. Y.; Gao, X. L.; Ding, S. R.** 2018. Band gaps for wave propagation in 2-D periodic composite structures incorporating microstructure effects, *Acta. Mech.* 229: 4199-4214. <https://doi.org/10.1007/s00707-018-2207-2>.
23. **Zhang, G. Y.; Gao, X. L.** 2019. Band gaps for flexural elastic wave propagation in periodic composite plate structures based on a non-classical Mindlin plate model incorporating microstructure and surface energy effects. *Continuum, Mech. Therm.* 31: 1911-1930. <https://doi.org/10.1007/s00161-019-00771-5>.
24. **Zhang, G. Y.; Zheng, C. Y.; Qiu, X. Y.; Mi, C. W.** 2021. Microstructure-dependent band gaps for elastic wave propagation in a periodic microbeam structure, *Acta Mech Sin.* 34: 527-538. <https://doi.org/10.1007/s10338-021-00217-z>.

25. **Hong, J.; He, Z.; Zhang, G.; Mi, C.** 2021. Tunable bandgaps in phononic crystal microbeams based on microstructure, piezo and temperature Effects, *Crystals* 11: 1029.
<https://doi.org/10.3390/cryst11091029>.
26. **Xia, Z. X.; Zhang, G. Y.; Cong, Y.; Gu, S. T.** 2022. A non-classical couple stress based Mindlin plate finite element framework for tuning band gaps of periodic composite micro plates, *J. Sound. Vib.* 529: 116889.
<https://doi.org/10.1016/j.jsv.2022.116889>.
27. **Lai, P. Y.; He, Z. Z.; Cong, Y.; Gu, S. T.; Zhang, G. Y.** 2022. Bandgap Analysis of Periodic Composite Microplates with Curvature-Based Flexoelectricity: A Finite Element Approach, *Acta Mech Sin.* 35: 996-1003.
<https://doi.org/10.1007/s10338-022-00359-8>.
28. **Argyris, J. H.; Fried, I.; Scharpf, D. W.** 1968. The TUBA family of plate elements for the matrix displacement method, *Aeronaut. J.* 72: 701-709.
<https://doi.org/10.1017/S000192400008489X>.
29. **Bell, K.** 1969. A refined triangular plate bending finite element, *Int. J. Numer. Meth. Eng.* 1: 101-122.
<https://doi.org/10.1002/nme.1620010108>.
30. **Clough, R. W.** 1965. Finite element stiffness matrices for analysis of plate bending, *Proc. of the First Conf. on Matrix Methods in Struct. Mech.*, p. 515-546. Available from Internet: <https://www.researchgate.net/publication/242360771>.
31. **Powell, M. J. D.; Sabin, M. A.** 1977. Piecewise quadratic approximations on triangles, *Acm. T. Math. Software* 3: 316-325.
<http://dx.doi.org/10.1145/355759.355761>.
32. **Hughes, T.; Cottrell, J.; Bazilevs, Y.** 2005. Isogeometric analysis: CAD, finite elements, NURBS, exact geometry and mesh refinement, *Comput. Methods Appl. Mech. Eng.* 194: 4135-95.
<http://dx.doi.org/10.1016/j.cma.2004.10.008>.
33. **Cottrell, J.; Hughes, T.; Bazilevs, Y.** 2009. *Isogeometric analysis: toward integration of CAD and FEA*, John Wiley. & Sons. Inc.
<http://dx.doi.org/10.1002/9780470749081.ch7>.
34. **Kittel, C.; McEuen, P.; McEuen, P.** 1996. *Introduction to solid state physics*. New York: Wiley.
<http://dx.doi.org/10.1063/1.3060399>
35. **Yang, F.; Chong, A. C. M.; Lam, D. C. C.; Tong, P.** 2002. Couple stress based strain gradient theory for elasticity, *Int. J. Solids. Struct.* 39: 2731-2743.
[http://dx.doi.org/10.1016/S0020-7683\(02\)00152-X](http://dx.doi.org/10.1016/S0020-7683(02)00152-X).
36. **Ma, H. M.; Gao, X. L.; Reddy, J. N.** 2011. A non-classical Mindlin plate model based on a modified couple stress theory, *Acta. Mech.* 220: 217-235.
<http://dx.doi.org/10.1007/s00707-011-0480-4>.
37. **Zhang, G. Y.; Qu, Y. L.; Gao, X. L.; Jin, F.** 2020. A transversely isotropic magneto-electro-elastic Timoshenko beam model incorporating microstructure and foundation effects, *Mech. Mater.* 149: 103412.
<http://dx.doi.org/10.1016/j.mechmat.2020.103412>.
38. **Mindlin, R. D.** 1951. Influence of rotatory inertia and shear on flexural motions of isotropic, elastic plates, *Int. J. Appl. Mech.* 1: 31-38.
<http://dx.doi.org/10.1115/1.4010217>.
39. **Ghorashi, S. S.; Valizadeh, N.; Mohammadi, S.** 2012. Extended isogeometric analysis for simulation of stationary and propagating cracks, *Int. J. Numer. Meth. Eng.* 89(9): 1069-1101.
<http://dx.doi.org/10.1002/nme.3277>.
40. **Yin, S. H.; Yu, T. T.; Bui, T. Q.; Zheng, X. J.; Gu, S. T.** 2019. Static and dynamic fracture analysis in elastic solids using a multiscale extended isogeometric analysis, *Eng. Fract. Mech.* 207: 109-130.
<https://doi.org/10.1016/j.engfracmech.2018.12.024>.
41. **Lam, D. C. C.; Yang, F.; Chong, A. C. M.; Wang, J.; Tong, P.** 2003. Experiments and theory in strain gradient elasticity, *J. Mech. Phys. Solids.* 51: 1477-1508.
[https://doi.org/10.1016/S0022-5096\(03\)00053-X](https://doi.org/10.1016/S0022-5096(03)00053-X).
42. **Park, S. K.; Gao, X. L.** 2006. Bernoulli-Euler beam model based on a modified couple stress theory, *J. Micro-mech. Microeng.* 16: 2355-2359.
<https://doi.org/10.1088/0960-1317/16/11/01.5>.

P. Liu, J. Zhou, S. Yin, Y. Mei

VIBRATION BANDGAP ANALYSIS OF PERIODIC COMPOSITE MICROPLATES USING ISOGEOMETRIC APPROACH

S u m m a r y

For periodic composite microplates, the microstructure dependent effect has great influence on the elastic wave vibration band gaps. In this paper, an effective isogeometric analysis method based on the modified couple stress theory (MCST) is proposed to calculate the vibration band gaps in periodic composite microplates. The MCST is employed to capture the microstructure effect of vibration band gaps in periodic composite microplates. The high order continuity requirement of MCST can be easily satisfied by applying the NURBS based isogeometric analysis approach. The elasto-dynamics and discrete equations of isogeometric analysis are obtained under the Mindlin kinematics assumptions. The present approach is validated by comparison with the analytical solution. And the influence of microstructure effect, volume fraction and unit cell length on the band gaps are investigated in details.

Keywords: band gaps, isogeometric analysis, microstructure effect, modified couple stress theory, mindlin plate.

Received April 4, 2023

Accepted December 3, 2023



This article is an Open Access article distributed under the terms and conditions of the Creative Commons Attribution 4.0 (CC BY 4.0) License (<http://creativecommons.org/licenses/by/4.0/>).